Chapter 6
Phonons in Thin Oxide Films

Luca Vattuone, Letizia Savio and Mario Rocca

Abstract Thin oxide films have physical and chemical properties which may be significantly different from those of the corresponding bulk materials. For their complete characterization the information on the lattice dynamics which can be retrieved by vibrational spectroscopy is mandatory. Here we show that the number of observed phonon modes and their frequencies can indeed provide relevant information about stoichiometry, structure and thickness of the film.

6.1 Introduction

In recent years an increasing number of studies has been devoted to the characterization of the properties of thin oxide films. A film can be considered to be "thin" as long as the size of its single crystalline domains in the plane of the surface strongly exceeds its thickness. The term "ultrathin" is used, on the other hand, when the latter goes from one to just a few atomic layers. In the opposite limit, when the extension along all three dimensions is comparable, it is more appropriate to consider the film as an agglomeration of nanoparticles. The interest in thin and ultrathin films is motivated by the following considerations:

(a) A thin oxide film is usually grown epitaxially on an appropriate single or poly-crystalline substrate, chosen so that the lattice mismatch with the corresponding bulk oxide is minimized. One could thus expect the thin film to be very close to what one could ideally obtain by cutting a slab from the bulk

L. Vattuone (✉) · M. Rocca
Dipartimento di Fisica dell'università di Genova, Via Dodecaneso 33, 16146 Genoa, Italy
e-mail: vattuone@fisica.unige.it

M. Rocca
e-mail: rocca@fisica.unige.it

L. Vattuone · L. Savio · M. Rocca
IMEM-CNR Unità Operativa di Genova, Via Dodecaneso 33, 16146 Genoa, Italy
e-mail: savio@fisica.unige.it

F.P. Netzer and A. Fortunelli (eds.), *Oxide Materials at the Two-Dimensional Limit*, Springer Series in Materials Science 234, DOI 10.1007/978-3-319-28332-6_6

solid. Reality is, however, often more complex. There is inevitably a few percent difference between the lattice spacing of the most appropriate substrate and the one of the bulk oxide. In the ultrathin limit the film is thus either slightly compressed or slightly strained, i.e. different from the ideal bulk-like slab depicted above. Such a difference may cause the film to show different electronic and chemical properties with respect to those expected for a surface layer obtained by cutting a bulk oxide [1]. Only after reaching thicknesses of some tens of layers, the lattice spacing attains the bulk limit value releasing the stress and reducing it to negligible values. In this limit we expect our film to behave in the same way as the bulk solid, except possibly for just the very first layers at the interface with the underlying substrate, and its surface to have properties quite similar to those of the one obtained by cutting the bulk oxide.

(b) The electronic structure of the substrate may directly affect the one of the thin film on top of it. For the most reactive cases, the deposition of the film can also modify the substrate by causing its reconstruction. The film itself or the atoms, the molecules and the clusters deposited on the surface can conversely behave differently depending on the influence of the substrate, i.e. on film thickness [2]. In some cases, charge transfer to particles supported on the oxide films may occur. Such charging depends on the electronic properties of the substrate and of the film and decreases with increasing film thickness. It has been shown that charging can affect the equilibrium shape of the nanoparticle as well as its chemical reactivity.

(c) Thin oxide films deposited on a conductive substrate still allow to use the powerful electron based spectroscopic tools typical of surface science, like X-ray photoelectron spectroscopy (XPS), Ultra violet Photoelectron Spectroscopy (UPS), High Resolution Electron Energy Loss Spectroscopy (HREELS) and Low Energy Electron Diffraction (LEED), just to mention the most widely employed. Since a large set of information regarding stoichiometry and oxidation state can be inferred only by such techniques, thin films represent an appealing model system for the characterization of the surfaces of insulating bulk oxides [3].

The aim of the present review is to show and discuss the vibrational spectra of thin films, from which a large amount of information on structure, stoichiometry and even morphology of the oxide layer can be inferred. To this purpose, we will not provide a comprehensive review but we will rather focus our attention on a few paradigmatic cases taken from the recent literature in the field. Since for an oxide film the number of observable vibrational modes, and hence the complexity of the spectra, is determined by its stoichiometry, we will firstly address simple oxides with only two atoms/cell such as MnO, MgO and NiO. We will then consider more complex materials such as TiO_2 and SiO_2 and move eventually to Al_2O_3 and Fe_3O_4. Whenever possible, we will present data obtained for different thicknesses of the films and try to correlate them with structural and stoichiometric information.

We will see that some modes have a microscopic character while other ones are macroscopic in nature. The former, addressed as Wallis modes, depend on the local

structure and force constants and can be predicted only using methods taking into account the real atomic structure and the actual forces between the atoms in the film. The latter, also called Fuchs-Kliewer (FK) modes [4], correspond to the relative motion of macroscopic cationic and anionic sub-lattices with respect to each other, and can be described in the frame of dielectric theory.

6.2 Power and Limits of Dielectric Theory

Dielectric theory enables one to predict the energy of vibrational modes for a bulk solid as well as for a film of given thickness [5]. For a single crystal and for a thick enough film, i.e. in the limit of bulk oxide surfaces, the energy of the FK mode (ω_{FK}) reads:

$$\hbar\omega_{FK} = \sqrt{\frac{\epsilon_0 + 1}{\epsilon_\infty + 1}}\hbar\omega_{TO} \tag{6.1}$$

where ω_{TO} is the frequency of the TO (i.e. zone centre transverse optical) phonon, ε_0 the static dielectric constant and ϵ_∞ the high frequency limit of the dielectric function.

For a film the energy of the FK mode depends on thickness. It is possible to define [6] an effective dielectric constant, $\xi_o(\boldsymbol{q}_\parallel, \omega, d)$ for a two layer system of thickness d in terms of the (frequency dependent) dielectric function of the oxide layer $\varepsilon(\omega)$ and of the substrate $\xi_s(\boldsymbol{q}_\parallel; \omega)$, which can be written as:

$$\xi_o(\boldsymbol{q}_\parallel, \omega, d) = \epsilon \coth(q_\parallel d) - \frac{\left(\frac{\epsilon}{\sinh(q_\parallel d)}\right)^2}{\epsilon \coth(q_\parallel d) + \xi_s(\boldsymbol{q}_\parallel, \omega)} \tag{6.2}$$

The dielectric function of the oxide layer is

$$\epsilon(\omega) = \epsilon_\infty + \frac{(\epsilon_0 - \epsilon_\infty)\omega_{TO}^2}{\omega_{TO}^2 - \omega^2 - i\gamma\omega\omega_{TO}} \tag{6.3}$$

where γ is the appropriate damping constant, while the dielectric function of the substrate can be written in a simplified Drude form (neglecting the dependence on the wavevector)

$$\xi_s(\omega) = \frac{-\omega_p^2}{\omega^2 + i\gamma_p\omega\omega_p} \tag{6.4}$$

where ω_p is the surface plasmon energy of the substrate and γ_p the damping factor. Using dielectric theory it is possible to compute also the loss function. Peaks are expected whenever $\xi = -1$ as shown in Fig. 6.1 [7, 8].

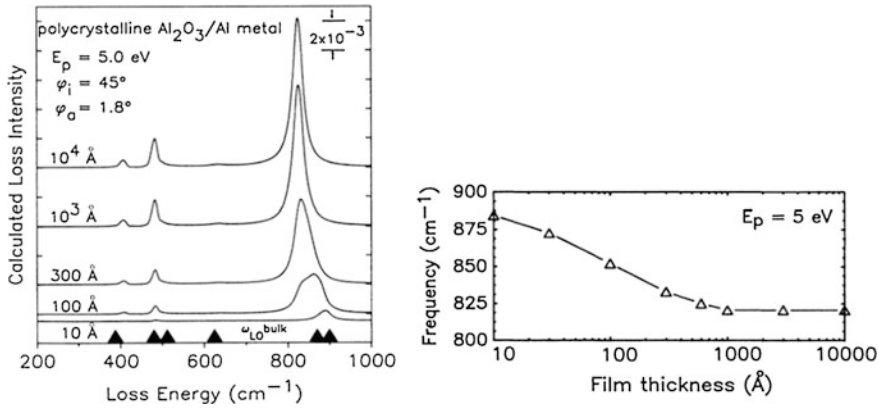

Fig. 6.1 *Left* Calculated HREEL spectra for polycrystalline Al_2O_3 films grown on Al for different thicknesses. *Right* Dependence of frequency on film thickness for the higher energy phonon. Taken with permission from [7]. Copyright by APS

As pointed out already in 1991 [8], dielectric theory becomes inadequate for thin films since the contribution of microscopic phonons is then no longer negligible and a microscopic theory becomes mandatory in order to reproduce the experimental results. In this limit also the distinction between macroscopic modes (predicted by dielectric theory) and microscopic ones may become fuzzy.

6.3 Brief Resume of Selection Rules for Vibrational Spectroscopy

Before showing selected results for a few systems of increasing complexity it is worth to briefly summarize the selection rules which are operative for HREELS and Infra-Red Absorption Spectroscopy (IRAS) on a metal substrate. The reader is referred to more specialized books [9] or reviews (see e.g. [10]) for a more comprehensive treatment [9].

According to quantum mechanics the vibrational transition probability is proportional to the square of the transition dipole moment:

$$\langle \mu \rangle = \int \Psi_f^*(Q_k)\mu\, \Psi_i(Q_k) dQ_k \tag{6.5}$$

where μ is the dipole moment operator of the molecule, Ψ_I and Ψ_f are the initial and final vibrational wave functions for the given normal mode with wavevector k and Q_k is the corresponding normal mode coordinate [10]. By expressing the dipole moment μ into its x, y and z coordinates we can easily conclude that at least one of these components must be non-vanishing for this mode to be IR active. We could

otherwise state that only vibrational transitions with a change in the dipole moment are IR active. The intensity I_k of band k will thus be proportional to $\left(\frac{d\mu}{dQ_k}\right)^2$. Using the general language of group theory it is necessary that the product $\Gamma_f \times \Gamma_\mu \times \Gamma_i$ of the representations of Ψ_f, μ and Ψ_i contains the totally symmetric representation.

For transitions from fundamental to first excited vibrational state (the most common case), since the initial state belongs to the totally symmetric representation [11], it is necessary that the final state belongs at least to the same representation of one of the components of μ. In less formal words, only vibrational modes which transform as one of the coordinates x, y or z can be excited by IR light.

If the substrate is a metal and if z is the coordinate normal to the surface, the selection rule is more restrictive and only dipole moments which transform as z can be active. This is the so-called metal selection rule which is usually shortly stated saying that only vibrational modes with a component of the dynamical dipole moment perpendicular to the metal surface will contribute to the IR absorbance. This rule can be understood qualitatively since the electric field parallel to the metal surface must vanish at least for frequencies lower than the plasma frequency of the metal, i.e. whenever a dipole parallel to the surface can be screened by the image dipole created by the conducting electrons in the metal.

In general, for any given space group it is possible to infer by inspection of the character table which modes are totally symmetric and then to know the number of expected IR active modes. Conversely, if the structure is not known or if there are alternative possibilities, the number of observed modes at least restricts the possible choices.

The situation is more complicated for HREELS. Under dipole scattering conditions, i.e. when the excitation of the surface vibration is caused by the electric field of the incoming electron, the same selection rules as for RAIRS apply. This is the usual case when inspecting spectra recorded in-specular, i.e. when the angle of incidence and of reflection of the electron beam are identical, so that the parallel momentum transfer is small compared to that of the incoming electrons. However for HREELS other scattering mechanisms are possible, namely impact and resonance scattering: such mechanisms are not affected by the dipole selection rule and allow to observe also vibrations which are not IR active. When these mechanisms dominate, the intensity may change with scattering angle non-monotonically and be significant for off-specular geometries. The use of impact and resonant scattering in the study of thin oxide films is limited since detailed theoretical calculations are needed to account for the angle and energy dependence of the scattering cross section. For this reason we will not discuss them further in this review [12, 13].

Finally, vibrational information can be obtained also by Surface Enhanced Raman Scattering, SERS. Similarly to RAIRS (and contrary to HREELS!) SERS does not require UHV conditions and can thus be employed also at atmospheric pressure and in reactive environments. At variance with RAIRS, the inelastic scattering of light has an inherently low cross section which severely limits its sensitivity except under special conditions associated to surface roughness. The selection rules for SERS are quite different from the ones of RAIRS and dipolar

HREELS: in order to be Raman active a vibrational transition must indeed cause a change in the polarizability (rather than a change in the dipole moment as for IRAS). Using the same formalism introduced above, for a transition from the fundamental to the first excited state to be Raman active it is necessary that the vibrational mode transforms as the product of two coordinates (e.g. xx, xy, xz, etc). The operator in (6.5) is now the polarizability tensor, while it was the dipole moment in the case of RAIRS. For this reason and with the only exception of crystals without center of inversion, a Raman active mode is inactive in RAIRS and viceversa [11].

Finally, we mention that the most common unit when dealing with IRAS and RS is the cm^{-1}, while for HREEL spectra are often expressed in meV. Since using a uniform notation would require to modify some of the original data, we recall here that the conversion factor between the two units is 1 meV = 8.065 cm^{-1}. We will report in the following the converted value in parenthesis next to the original value every time we feel it is necessary for an easier comparison between different experiments.

6.4 MeO Oxides Thin Films

6.4.1 MnO

Bulk MnO has a rock-salt structure with a lattice constant of 0.444 nm. MnO is an insulator with band gap between 3.6 and 4.3 eV and with antiferromagnetic behaviour below the Néel temperature of 118 K. Vibrational spectra for the bulk material show a transverse optical phonon (TO) at the $\bar{\Gamma}$ point having an energy of 265 cm^{-1} [14], which splits below 118 K due to the occurrence of magnetic ordering [15].

MnO films have been grown on different substrates (see [6] and references therein). In Fig. 6.2 we show the HREEL spectrum for MnO grown on Pt(111) by deposition of Mn in O_2 atmosphere at 375 K, parametric in film thickness (expressed in oxide monolayers, ML). Below the completion of the first ML, only one peak at 367 cm^{-1} (46 meV) is present. It shifts to higher energy with increasing thickness saturating at 382 cm^{-1} (47 meV). It is assigned to the Wallis mode, in which the first layer O atoms vibrate against the Mn lattice along the surface normal. The small change of the mode frequency with film thickness indicates its local character. A second peak at an energy of 547 cm^{-1} (68 meV) shows up only after completion of the first monolayer. Its intensity increases linearly with coverage and does not seem to saturate. This loss has been identified with the FK mode, a surface phonon polariton responsible for the dielectric response of MnO. The negatively charged oxygen lattice and the positively charged Mn lattice vibrate thereby with respect to each other in counter-phase. The FK mode frequency shows a slight decrease with increasing thickness, as predicted by dielectric theory.

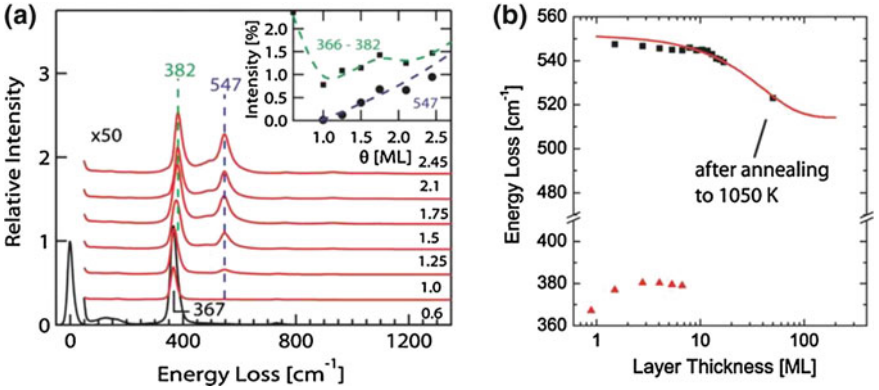

Fig. 6.2 *Left* HREEL spectra for MnO films on Pt(111). The *inset* shows the dependence of the peak intensities on thickness. The *dashed lines* are guide for the eye. *Right* Dependence of the frequency of the FK (*black squares*) and Wallis (*red triangles*) modes on the thickness of the oxide layer. Taken with permission from [6]. Copyright by APS

It is remarkable that the frequency of the FK mode depends not only on the MnO film thickness (i.e. number of layers, otherwise addressed as coverage) but also on its morphology. This result is evident from inspection of Fig. 6.3 showing the change in the HREEL spectra after annealing a 17 ML thick film of MnO/Pt(111). Up to 850 K, no qualitative changes occur in the HREEL spectra except for the decrease of the FK peak width, indicating a reordering of the film. On the contrary,

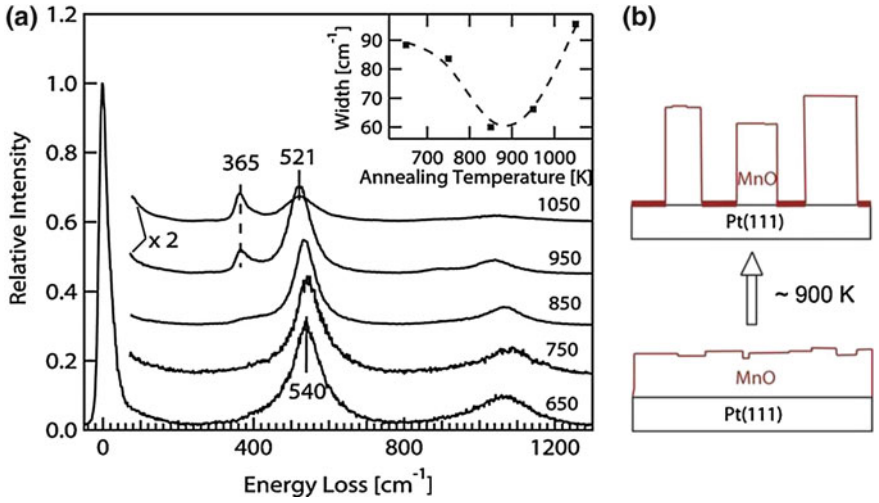

Fig. 6.3 *Left* HREEL spectra recorded after annealing a 17 ML thick film of MnO grown on Pt (111) at different temperatures. The *inset* shows the width of the FK peak while in the right part of the picture a schematic of the restructuring of films is shown. Taken with permission from [6]. Copyright by APS

annealing at higher temperature causes an increase in the width and a relatively large redshift (from 547 to 521 cm^{-1}, i.e. from 68 to 64 meV) of the FK mode, indicating a substantial restructuring of the MnO layer.

We note that the Wallis mode is not visible in the spectra of films thicker than 10 ML (see Figs. 6.2 and 6.3). In such conditions the mode is still there but its loss is embedded in the tail of the FK peak. It reappears only after annealing, when the intensity of the FK loss has decreased significantly. This behaviour is indicative of a restructuring of the surface (schematized in Fig. 6.3b). A large part of it is now covered by one monolayer thick MnO islands and, since the total amount of MnO cannot decrease, the remaining oxide must have reorganized in relatively thick clusters of 40–50 ML height. The authors estimate that, under the investigated experimental conditions, 2/3 of the surface is covered by monolayer MnO and 1/3 by thick clusters.

The oxidation of Mn can lead to the formation of oxides having a higher oxygen content than MnO. We will present vibrational data relative to them in paragraph 1.6.

6.4.2 MgO

In the case of MgO/Ag(100) the correlation between the vibrational frequencies and the morphology of the film is preserved and even amplified in the low coverage limit [16, 17]. We present the growth of MgO films of different thicknesses at the growth temperature T_g = 453 K in Fig. 6.4.

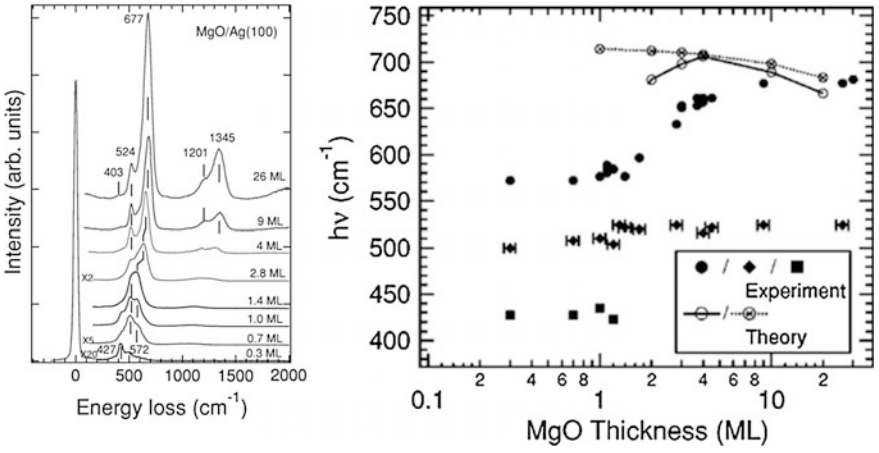

Fig. 6.4 *Left* HREEL spectra recorded after growing MgO films of different thicknesses on Ag (100) at 453 K. *Right* Dependence of observed vibrational frequencies on film thickness and comparison with the value predicted by theory for the FK mode. The *open circles* refer to the theoretical values for FK calculated using a microscopic approach (see [16] for details) while the crossed circles refer to the forecasts of dielectric continuum theory. Taken with permission from [16]. Copyright by APS

The spectra show a mode at 427 cm^{-1} (53 meV), which disappears upon the completion of the first layer, a mode around 524 cm^{-1} (64 meV), present for all films at the same frequency, and a mode around 670 cm^{-1} (83 meV), appearing only after completion of the monolayer and increasing in intensity with film thickness.

The low energy loss is assigned to a vibration at MgO sites at the edges of the islands in contact with Ag, since it disappears above 1 ML. Indeed STM inspection will show that, under the growth conditions applied in this experiment, sub-monolayer films consist of single layer islands of MgO with a quite irregular shape and thus a high density of borders. The loss at 524 cm^{-1} (64 meV) is identified with the Wallis mode, which is indeed expected to be little affected by thickness due to its microscopic nature. Finally, the mode at the highest frequency is assigned to the FK mode. In the thickness range between 0.7 and 1.4 ML, intensity is also present in the frequency range between 572 cm^{-1} (71 meV) and 605 cm^{-1} (75 meV).

Several growth procedures for monolayer MgO films on Ag(100) were tested, monitoring the film morphology by low temperature STM. It was found that both the usual growth parameters (T_g, oxygen pressure, Mg flux) and after growth treatments are important in determining the film structure [17], as evidenced in Fig. 6.5. When the film is grown at T_g = 450 K and the sample rapidly cooled down below room temperature (fast cooling procedure, FC), single layer MgO islands of irregular shape form (see line scans in Fig. 6.5e). If the growth temperature is increased to 773 K and the sample is again cooled down rapidly after growth, multilayer (mainly bilayer) islands with nice straight borders along the ⟨001⟩ direction are observed. Finally, if the film is grown at 773 K and subsequently cooled down slowly (slow cooling protocol, SC), flat terraces limited in size only by substrate steps are formed. This result can be explained by thermodynamic arguments: the surface energy of MgO and Ag(100) are respectively 1.15 and 1.20 J/m^2 so that entropy determines the favoured growth mode. At the lowest temperature a layer by layer growth is expected and in the low coverage limit islands of single layer thickness form to minimize the area of the uncovered Ag surface. At T_g = 773 K, due to entropy, a multilayer island growth mode is preferred: when the sample is rapidly cooled down, the morphology which is energetically favoured at this T_g is quenched and double or multilayer islands are observed. On the contrary, if the system is slowly cooled down, thus allowing it to attain its thermodynamically favoured morphology, nearly perfect single layer terraces are obtained.

It is interesting to see how the morphological information provided by STM correlates with the vibrational information obtained by HREELS (see Fig. 6.5f). The Wallis mode is always present, as expected. The mode at 53 meV (427 cm^{-1}) is best visible for T_g = 450 K and FC. In accord to its assignment to an MgO localised at the edges of the islands in contact with the substrate [16], it has a lower intensity when the film grown at 450 K is slowly cooled down, thus allowing the islands to attain a more regular shape and minimize the edge length. The mode at 75 meV (605 cm^{-1}), the intensity of which is largest for FC, i.e. when irregular edges are

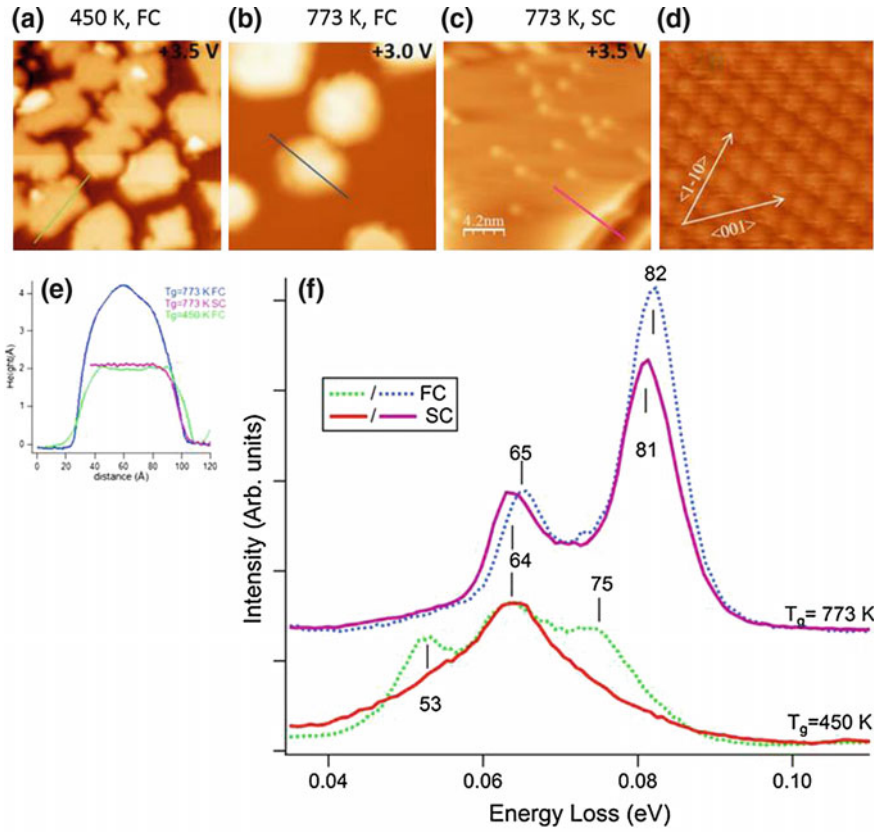

Fig. 6.5 *Top* (**a**–**c**) STM images recorded for different growth temperatures (450 and 773 K) and for different post growth treatments (*FC* fast cooling; *SC* slow cooling). Image size: 21 × 21 nm^2, I = 0.2 nA. We note that images are recorded at a bias voltage V ≥ 3.0 V, i.e. under topographical conditions. They are thus fully representative of the MgO layer geometry. **d** Atomically resolved image of clean Ag(100), used for calibration. High symmetry directions are marked by *arrows*. Image size 2.4×2.4 nm^2, V = 0.1 V, I = 0.2 nA. *Bottom* **e** Line scans along the directions marked in panels **a**, **b** and **c**. **f** HREEL spectra recorded for the different growth conditions. Taken with permission from [17]. Copyright by APS

present, has been assigned to microscopic modes different from the Wallis one and involving the motion of oxygen at the border of the islands. Indeed its width is indicative for the presence of several different contributions in the range of frequencies between 71 and 75 meV (572–605 cm^{-1}), whose weight depends on the details of the local environment.

More importantly, the FK mode, expected around 82 meV (661 cm^{-1}), is not observed here since it can only exist in areas covered by at least one layer. This mode is, indeed, well evident for the only case in which bilayer islands formation occurs, i.e. T_g = 773 K and FC.

There remains to explain why for T_g = 773 K and SC, when STM inspection shows only extended and nearly perfect single layer terraces, the FK mode persists, although with a slightly red shifted frequency (81 meV, 653 cm^{-1}). The reason is that in these conditions the film is over-stoichiometric in oxygen, as demonstrated by XPS [18]. The excess oxygen atoms accumulate at the interface and allow to release the stress present at the interface, definitely favouring the formation of the large single layer terraces observed by STM images. The 81 meV mode can thus be assigned to the counter-phase vibration of the Mg sub-lattice against the O atoms of the oxide film plus those of the incomplete interface oxygen layer, resulting in a FK-like motion.

MgO is usually grown on Ag(100) or Mo(100) but growth on TiC(100) has been tried, too [19]. For a two layer film, frequencies of 65 meV (524 cm^{-1}) and 86 meV (694 cm^{-1}) have been observed for the Wallis and FK modes, respectively. The Wallis mode has thus the same frequency observed for the other substrates, while the frequency of the FK mode is slightly higher than for MgO double layers on Ag (100). The better agreement with dielectric theory indicates a very good quality of the film structure.

6.4.3 NiO

Similar experiments have been performed for NiO thin films grown on Pd((100) or on Ni(111) [20, 21]. On Pd(100) the first layer consists thereby of a slightly distorted NiO(100) sheet with Ni vacancies arranged in an ordered $c(4 \times 2)$ array resulting in a Ni_3O_4 stoichiometry. Oxygen sits on-top of the Pd atoms, while Ni occupies the FFH sites. In such conditions only a single loss at 46 meV is observed in-specular with HREELS, see Fig. 6.6 bottom spectrum. When increasing the coverage, a peak at 64 meV (shifting to 68 meV with film thickness) appears as soon as the second layer forms, corresponding to the FK mode of NiO (to be compared with 69.5 meV for the bulk crystal) [22]. The loss at 46 meV redshifts to 42 meV and becomes hardly visible. Another (weak) peak is present at 52 meV, the origin of which is still unclear [20, 21]. The decrease in the FK frequency with film thickness predicted by dielectric theory becomes evident only at higher coverage.

NiO has been grown also on Ni(111) [21]. In such case the FK mode appears at 510 cm^{-1} (63 meV) in the low thickness limit.

6.5 MeO_2 and Me_2O_3 Thin Films

When considering oxides with more atoms per unit cell, the picture becomes more complex since the number of normal modes increases. We will consider here two examples: TiO_2 and SiO_2.

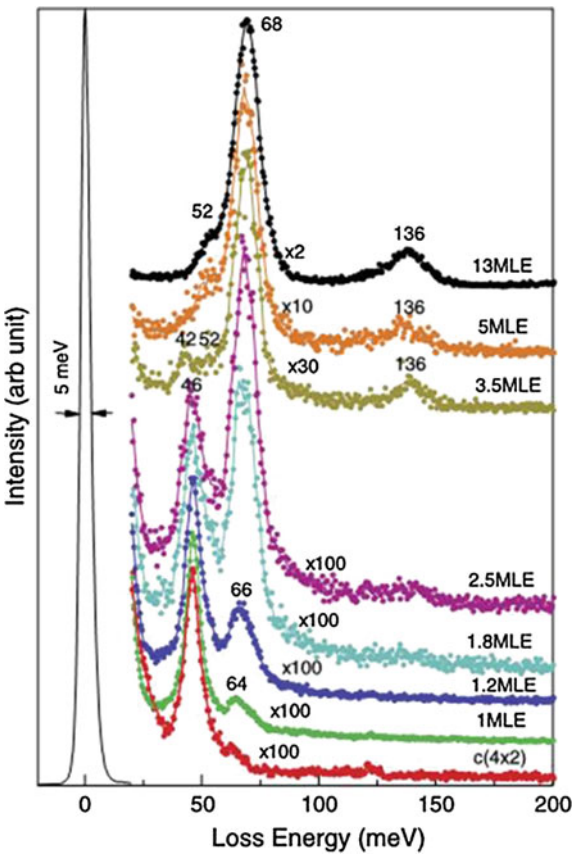

Fig. 6.6 HREEL spectra of Ni oxide grown on Pd(100) versus thickness. Taken with permission from [20]. Copyright by Elsevier

6.5.1 TiO_2 and Ti_2O_3

The interest for titania films has been boosted by the relevance of this material in several applications because of its biocompatibility. Titanium oxide exists in different stoichiometries and structures:

(a) TiO, having NaCl structure and lattice constant of 0.423 nm;
(b) TiO_2, which can have three different structures:

1. brookite: orthorombic with lattice constants of 0.916 and 0.513 nm;
2. rutile: tetragonal with lattice constants of 0.459 and 0.296 nm;
3. anatase: tetragonal as well, but with lattice constants of 0.378 and 0.952 nm.

(c) Ti_2O_3, which has corundum structure with lattice constant 0.515 nm.

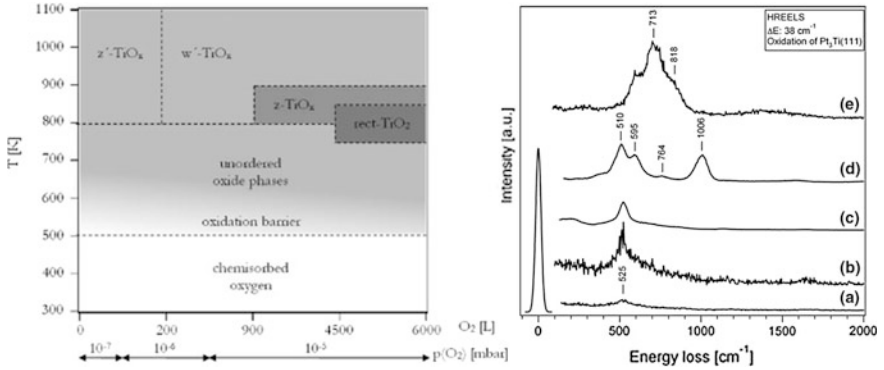

Fig. 6.7 *Left* Experimental phase diagram of the system $O_2/Pt_3Ti(111)$. Note that the abscissa is not linear. *Right* HREEL spectra recorded for different oxygen exposures: **a** 5 L O_2 at 1000 K, **b** 55 L O_2 at 1000 K, **c** 200 L O_2 at 1000 K, **d** 900 L O_2 at 900 K and **e** 4500 L O_2 at 800 K. The spectra **a** and **b** correspond to the $(6 \times 3\sqrt{3})$ phase, spectrum **c** to the $(7 \times 7)R21.8°$ layer, spectra **d** and **e** to the incommensurate rectangular and rotated rectangular structures, respectively. Taken with permission from [23]. DOI: http://dx.doi.org/10.1088/0953-8984/25/4/045013

The right panel of Fig. 6.7 shows HREEL spectra recorded during the oxidation of a $Pt_3Ti(111)$ surface [23]. Four different phases are observed (see also phase diagram in Fig. 6.7 left panel): the $(6 \times 3\sqrt{3})$ phase (also addressed as z' because of its zig zag shape) and the $(7 \times 7)R21.8°$ phase (indicated as w', where w stands for wagon wheel), obtained upon oxidation at 1000 K, are the most stable ones; the two incommensurate rectangular phases obtained at lower temperature and higher oxygen doses are, on the contrary, metastable.

Notably the commensurate z' and w' phases exhibit a similar phonon spectrum characterised by a single prominent loss at 525 cm^{-1} (65 meV). The presence of one single loss is indicative that both of them have a TiO stoichiometry. A single loss with close values of vibrational frequency is indeed observed for MnO (572 cm^{-1}, 71 meV [24]), NiO (569 cm^{-1}, 71 meV [25]) and CoO (560 cm^{-1}, 69 meV, [26]).

The incommensurate phases exhibit more complex spectra with losses at 510 cm^{-1} (63 meV), 595 cm^{-1} (74 meV), 764 cm^{-1} (95 meV) and 1066 cm^{-1} (132 meV) (rectangular phase) and at 595 cm^{-1} (74 meV), 713 cm^{-1} (88 meV) and 818 cm^{-1} (101 meV) (rotated rectangular phase), respectively. The vibrational spectrum rules out a TiO stoichiometry for these phases. The observed frequencies, however, cannot be assigned (or assimilated) to any of the existing bulk structures, since they are different from those reported for bulk Ti_2O_3 (379 cm^{-1} and 709 cm^{-1} (47 and 88 meV), [27]) and for both phases of TiO_2 (rutile: 365, 445 and 755 cm^{-1} (45, 55 and 93 meV), respectively [28]; anatase: 355 and 790 cm^{-1} (44 and 98 meV), respectively [29]). This result supports the widely accepted idea that new phases having no direct bulk equivalent do form at surfaces and that vibrational spectroscopy provides a nearly unique tool to identify such novel oxides with potentially unexpected and useful properties.

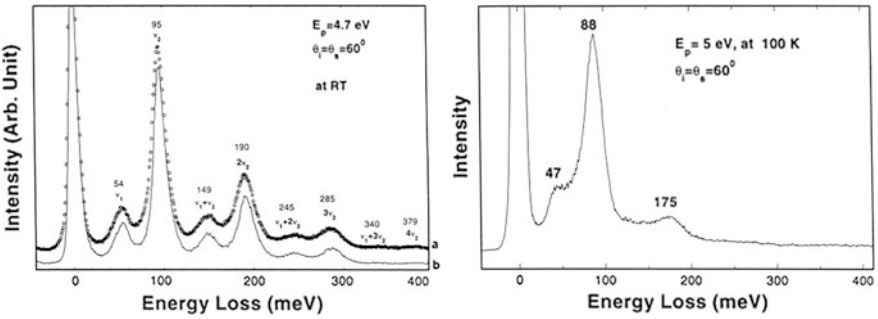

Fig. 6.8 HREEL spectra of titanium oxide films grown on Mo(110). *Left panel* Growth procedure with protocol I (30 ML thickness, recorded at RT, *upper trace*). The spectrum is compared to the one of a TiO_2(110) single crystal recorded at the same primary beam energy of 4.7 eV (*lower trace*). *Right panel* Film grown with protocol II (40 ML thickness, annealed to 1100 K, recorded at 100 K with primary energy of 5 eV). Taken with permission from [27]. Copyright by Elsevier

Titanium oxide films can also be grown on Mo(110) [27]. Films with different stoichiometry are obtained depending on the growth protocol. TiO_2 is obtained by evaporation of Ti under O_2 pressure (2.6×10^{-7} mbar) while keeping the substrate at 600–700 K and subsequent annealing to 800 K first in oxygen atmosphere and then in vacuum (protocol I). If, alternatively, some Ti (less than 1 ML) is deposited on the substrate in vacuum, continuing thereafter to grow the film following protocol I, an oxide layer with Ti_2O_3 stoichiometry forms (protocol II). The assignments of the structures was based on LEED, XPS and Auger Electron Spectroscopy, but valuable information is also provided by vibrational spectroscopy. Figure 6.8 shows HREEL spectra for films obtained with protocols I and II. Using protocol I, the HREEL spectrum is dominated by phonons at 54 and 95 meV and by their overtones. Such values are close to those measured [28] for rutile, which are reported for comparison. For protocol II the spectrum is dominated by losses at 47 and 88 meV and by one of their overtones. Such values are different both from those of films grown with protocol I and from those of bulk rutile [28] and anatase [29] samples; they are, however, similar to the peaks found for an ordered V_2O_3 film having corundum structure (see [27], main loss at 78 meV at 100 K and at 82 meV at 300 K). The frequencies obtained for Ti_2O_3 are thereby lower than for V_2O_3 because of the lower mass of Ti.

6.5.2 SiO_2

SiO_2 has also been widely investigated because of its technological importance. Single crystal SiO_2 films have been grown succesfully on Mo(112) [30–32]. Vibrational spectra, recorded both by HREELS and IRAS, show a main peak at 1048 cm^{-1} (130 meV), for which controversial assignments have been given. Chen

et al. [30] attributed it to the Si-O-Mo stretching vibration and, due to the absence of the Si–O–Si peak expected at 1176 cm^{-1} (146 meV), they concluded that the film consisted mainly of SiO_4 clusters. Kaya et al. [32] used the dipole selection rules to demonstrate that, for a 2D network of SiO_2, the Si–O–Si stretching vibration is not dipole active and thus cannot be detected by IRAS. Therefore, the absence of such mode in IRAS does not imply automatically the absence of Si–O–Si bonds. By using the same selection rules they could conclude that a 2D network can account for all the observed modes: indeed there are only three vibrations observable under dipole scattering conditions, namely the in-phase Si–O–Mo asymmetric mode (1061 cm^{-1}, 132 meV), and the out of phase and in phase couplings of symmetric Si–O–Si stretching modes (at 779 and 672 cm^{-1}, 97 and 83 meV respectively) as shown in Fig. 6.9. This result stems from the elegant application of the concepts of group theory described above.

Joining the vibrational information with STM and photoemission data, Kaya et al. further concluded that ultrathin silica film on Mo(112) consists of a two dimensional network of SiO_4 tetrahedra sharing the corner with one oxygen atom bonded with the substrate. For oxygen rich films a further oxygen moiety bonded directly to the substrate may be also present (see Fig. 6.10).

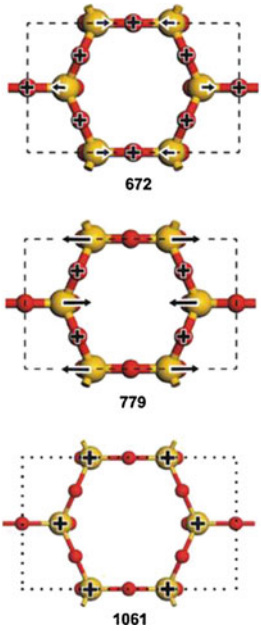

Modes (cm^{-1})	E	C_2	$\sigma(xz)$	$\sigma(yz)$	$1/2\tau$	C_2'	$\sigma'(xz)$	$\sigma'(yz)$
Asymmetric Si–O–Si								
$v_1 = 1195$	1	−1	−1	1	−1	1	1	−1
$v_2 = 1137$	1	−1	−1	1	1	−1	−1	1
$v_3 = 1092$	1	1	1	1	−1	−1	−1	−1
$v_4 = 1018$	1	−1	−1	1	1	−1	−1	1
$v_5 = 1010$	1	−1	1	−1	1	−1	1	−1
$v_6 = 1008$	1	1	−1	−1	−1	−1	1	1
Asymmetric Si–O–Mo								
$v_1 = 1061$	1	1	1	1	1	1	1	1
$v_2 = 912$	1	−1	−1	1	−1	1	1	−1
$v_3 = 881$	1	1	1	1	−1	−1	−1	−1
$v_4 = 863$	1	−1	−1	1	1	−1	−1	1
Symmetric Si–O–Si								
$v_1 = 821$	1	−1	1	−1	−1	1	−1	1
$v_2 = 817$	1	1	−1	−1	1	1	−1	−1
$v_3 = 779$	1	1	1	1	1	1	1	1
$v_4 = 695$	1	−1	−1	1	−1	1	1	−1
$v_5 = 676$	1	1	1	1	−1	−1	−1	−1
$v_6 = 672$	1	1	1	1	1	1	1	1

E: identity; C_2: twofold symmetry axis; $\sigma(xz)$: symmetry plane; $\sigma'(xz)$: glide plane; τ: translational period.

Fig. 6.9 *Left* Schematics of the eigenvectors of the three IR active modes of SiO_2/Mo discussed in the text (frequency in cm^{-1}). *Right* Table showing the symmetry properties of each mode with respect to the elements of the *cmm* group. Only totally symmetric vibrations (having thus "1" for all the columns of the same row) are IR active. Taken with permission from [32]. Copyright by Elsevier

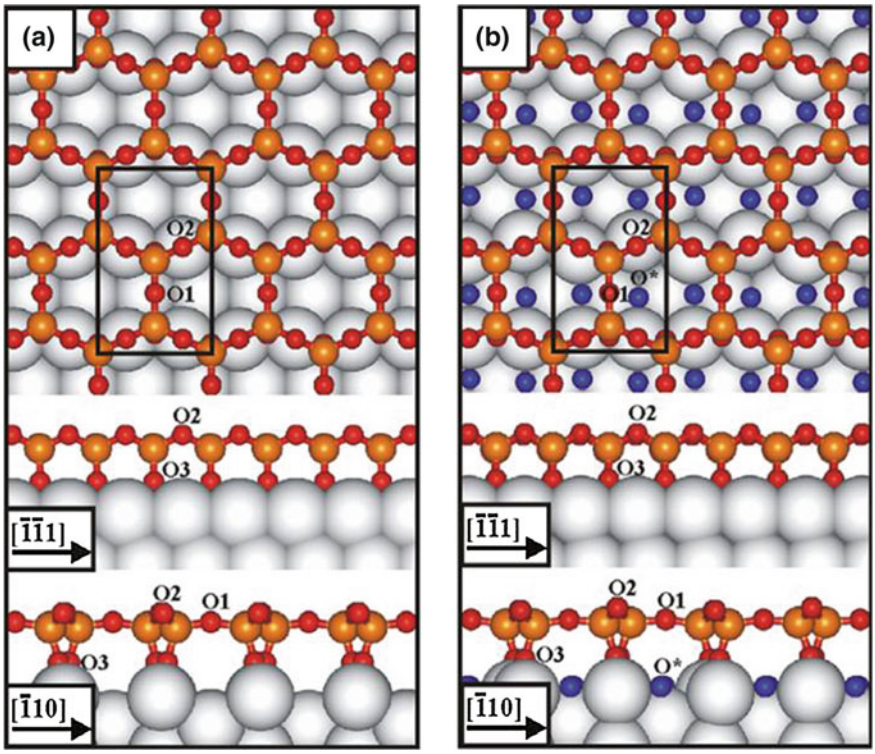

Fig. 6.10 Schematic of the 2D network model for the monolayer silica film grown on Mo(112). **a** O poor film and **b** O rich film. The additional O atoms (in *blue*) end up at the interface. Taken with permission from [32]. Copyright by Elsevier

The evolution of the vibrational spectra during growth and the subsequent annealing are shown in Fig. 6.11 [33]. We note that the modes expected according to the previous analysis definitely show up only after annealing the film (spectrum 8), i.e. when an ordered film has formed. The spectra recorded during growth are more complex. The mode at 675 cm^{-1} (84 meV) has been assigned to a Mo–O vibration involving oxygen atoms at the metal-oxide interface. The small band around 850 cm^{-1} (105 meV) corresponds to the symmetric Si–O stretch, while the asymmetric stretch modes in the region between 950 and 1250 cm^{-1} (i.e. between 118 and 155 meV) are intense and dominate the spectrum. The sharp peak at 987 cm^{-1} (122 meV) is assigned to the bending of Si–OH groups, as testified by the presence of the OH stretch mode at 3748 cm^{-1} (465 meV) (lower panel). The mode at 1022 cm^{-1} is assigned to a pseudomorphic SiO_2 layer at the interface. During growth the intensity of the high frequency shoulder at 1190 cm^{-1} increases and blue-shifts to 1218 cm^{-1} (151 meV). This effect was attributed to a decreased coupling of the film with the substrate due to the increased thickness. Another not identified shoulder shows up at 1155 cm^{-1} (143 meV). The richness of asymmetric

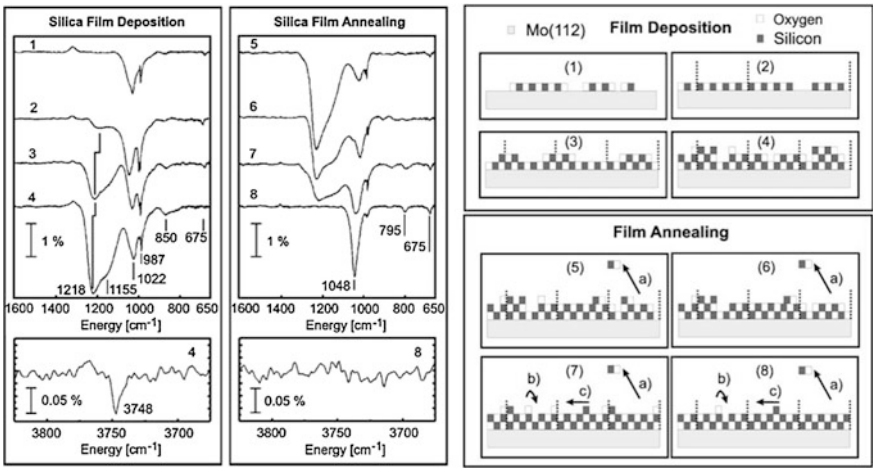

Fig. 6.11 *Left* IRA spectra recorded during growth of a silica film (1–4) and during annealing (5–8). The *bottom spectra* correspond to the frequency range of OH vibrations which indicate some OH contamination before annealing. *Right* Schematic of the suggested evolution of the layer during deposition and annealing. Taken with permission from [33]. Copyright by APS

Si–O modes is strongly indicative of the presence of different sites and thus of an increased corrugation of the film.

Upon annealing, the bands at 1155 cm^{-1} and at 1218 cm^{-1} disappear (see right panel, spectrum 8), leaving only an intense feature at 1048 cm^{-1} (130 meV) and small features in the low frequency region of the spectrum. Inspection of vibration spectra provides important hints about the growth mode, which are confirmed by LEED and Spot Profile Analysis-LEED investigations in the same multi-technique study [33].

The potential of vibrational spectroscopy is nicely demonstrated in Fig. 6.12 where the vibrational spectrum recorded for the 2D silica film is compared to the one of 1D stripes [34]. The mode at 1059 cm^{-1} (131 meV) is slightly red-shifted for the latter system, in agreement with the theoretical prediction (see bars in the highest part of Fig. 6.12). More important for the present context, the mode at 770 cm^{-1} (95 meV) blue-shifts to 875 cm^{-1} (108 meV) while the mode at 675 cm^{-1} (84 meV) remains almost unaffected. This result can be explained by the fact that in 1D stripes the Si–O–Si mode at 875 cm^{-1} is essentially a symmetric stretch vibration and has thus a higher frequency than the mode observed at 770 cm^{-1} for the 2D film, in which bending of the Si–O bond occurs. On the contrary, the Mo–O stretch vibration at 675 cm^{-1} does not change appreciably when changing the dimensionality of the layer.

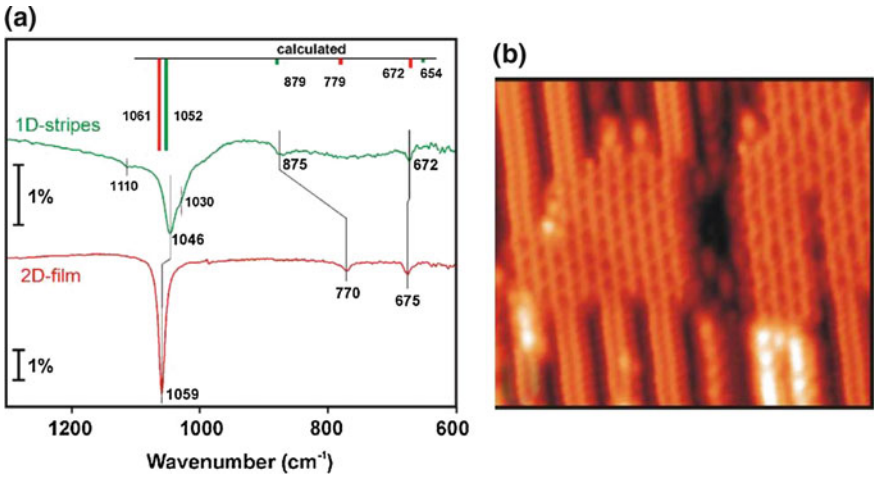

Fig. 6.12 **a** IRA spectra comparing 1D and 2D silica films. 1D stripes are obtained at submonolayer Si coverage [32]. When the silica stripes coalesce, particularly at increasing Si coverage, islands exhibiting a honeycomb-like structure are formed [34]. **b** STM image showing both stripes and island of silica film with atomic resolution (12.5 × 10.5 nm^2, −0.4 V, 0.4 nA). Taken with permission from [34]. Copyright by Elsevier

6.5.3 Al_2O_3

Together with titanium oxide, Al_2O_3 (alumina) is one of the most widely studied oxides because of its use as a support in catalysis. As already noted by Frank et al. [35], by monitoring frequency and intensity of the transverse optical (TO) and longitudinal optical (LO) phonons with IRAS it is possible to gather information on thickness and stoichiometry of such films. The ultimate reason for this is the so-called 'Berreman effect': in bulk dielectrics infrared adsorption occurs only at the frequencies corresponding to the TO phonon modes because of the transverse nature of electromagnetic waves. For films, on the contrary, also features close to the LO phonon modes are excited, provided that spectra are recorded using *p* polarized light at an oblique angle of incidence [36], thanks to the coupling to the component of the electric field normal to the surface.

For a dielectric slab on a metallic substrate it is therefore expected to observe IRAS features close to the LO frequencies of the related bulk solid. Transverse modes cannot be excited for a very thin film on a metal substrate since at a metal surface the electric field in the direction parallel to the interface vanishes. When measuring a vibrational spectrum by HREELS under dipole scattering conditions we expect to observe the same modes as in IRAS.

Al_2O_3 films can be grown on NiAl surfaces as shown first by Franchy [37]. The main information about FK modes and film structure are reported in Table 6.1. Depending on the phase formed, three to four FK modes are present.

Table 6.1 Vibrational frequencies of Fuchs-Kliewer modes and structure for alumina films on different NiAl surfaces. Data taken from [37].

Oxide and substrate	Fuchs Kliewer modes cm^{-1}	Structure
Al_2O_3/NiAl(100)	420, 603, 718, 896	θ-Al_2O_3
Al_2O_3/NiAl(110)	410, 620, 850	γ-Al_2O_3
Al_2O_3/NiAl(111)	427, 637, 887	γ-Al_2O_3 for T < 1000 K
		α-Al_2O_3 for T > 1100 K

In Fig. 6.13 IRA and HREEL spectra are compared for an alumina film grown on NiAl(110) [35]. A main feature at 860–870 cm^{-1} (107−108 meV) is observed in IRAS together with lower intensity features at 622 cm^{-1} (77 meV) and 660 cm^{-1} (82 meV). The HREEL spectrum is richer. Another intense mode is present at 419 cm^{-1} (52 meV), while additional fainter losses corresponding to microscopic modes are apparent, too. Such modes, not predicted by macroscopic dielectric theory, are expected to become more and more important with decreasing film thickness. Their assignment is, however, still controversial [38, 39].

In general, different phases can be obtained by oxidising a given substrate using different protocols. Vibrational spectroscopy can be used to distinguish among them. As summarized in Table 6.1, the γ phase is evidenced by the presence of three losses. It forms on NiAl(110) (frequencies at 410, 620 and 850 cm^{-1} (51, 77, 105 meV,

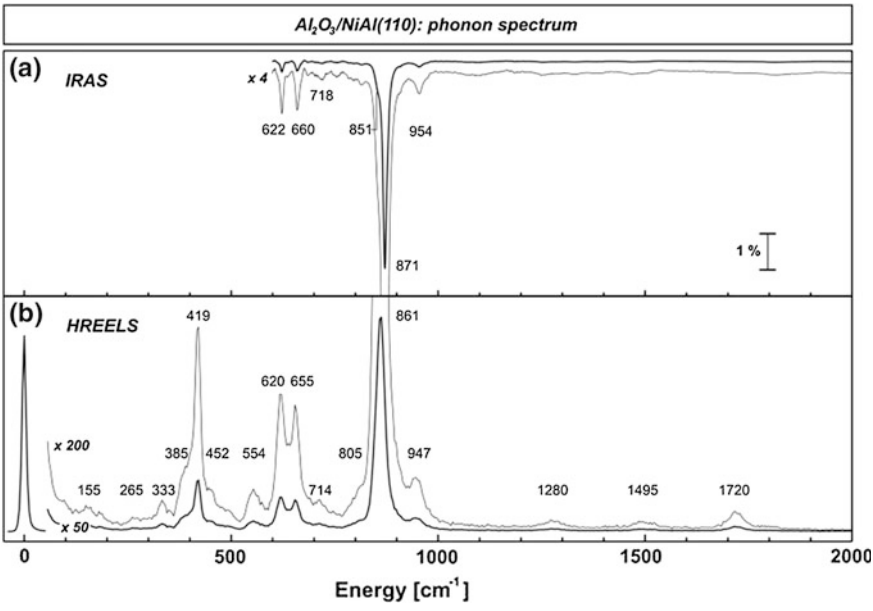

Fig. 6.13 IRA and HREEL spectra recorded at 90 K for alumina films grown on NiAl(110). Taken with permission from [35]. Copyright by Elsevier

respectively)) and on on NiAl(111) below 1000 K [frequencies at 427, 637 and 887 cm^{-1} (53, 79, 110 meV, respectively)]. The θ phase is, on the contrary, characterised by four losses. It forms on NiAl(100) where peaks at 420, 603, 718 and 896 cm^{-1} (52, 75, 89 and 111 meV, respectively) are observed. Annealing the γ phase grown on NiAl(111) above 1100 K the α-phase is obtained, characterised by losses at 78 and 113 meV [40]. Such phase forms also by oxidising NiAl(100) at 1400 K [41]. Losses at 638 and 913 cm^{-1} (79 and 113 meV, respectively) are then observed.

6.5.4 V_2O_3

Moving to vanadia, V_2O_3 thin films have been grown both on Rh(111) [42] and on TiO_2(110) (1 × 1) and (1 × 2) surfaces [43, 44]. Surface terminations for the (0001) surface of V_2O_3 with corundum structure have also been investigated by DFT [45], finding that three ideal bulk terminations are possible for the (0001) surface: (a) oxygen termination by an O_3 layer, (b) vanadium termination by a V_2 bilayer and (c) vanadium termination by a single V layer. According to DFT, termination (a) is favoured under oxygen rich conditions, termination (b) is highly unstable and (c) can occur only under highly reducing conditions. The thermodynamically stable

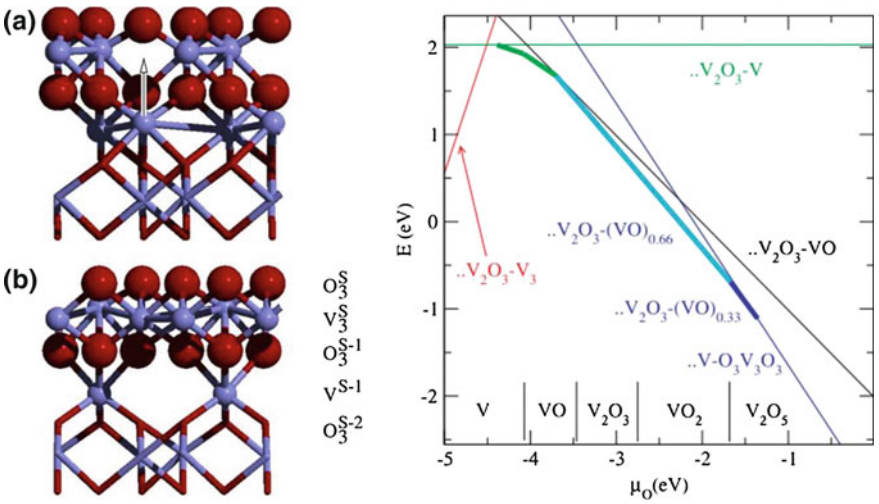

Fig. 6.14 *Left* Schematics showing the ideal V_2O_3 termination (**a**) and the energetically most stable termination (**b**) obtained by moving a vanadium atom from the second V_2 layer (S − 1) to the surface V_2 layer. *Right* Surface energy per primitive surface cell versus chemical potential μ_0 of oxygen for the (0001) surface of rhombohedral V_2O_3. *Thin lines* correspond to calculations for the primitive unit surface cell, *thick shorter lines* correspond to reconstructed cells with a periodicity of $(\sqrt{3} \times \sqrt{3})R30°$. The *thick lines* between V_2O_3V and V_2O_3VO indicate mixed $V_2O_3V_x(VO)_{1-x}1$ phases. The stability range of the bulk oxides are indicated at the *bottom* of the graph. Taken with permission from [45]. Copyright by Elsevier

O_3 termination is, however, not simply a continuation of the bulk corundum structure and a complex relaxation resulting into a—V_2O_3–V–$O_3V_3O_3$ stacking sequence occurs at the surface (see Fig. 6.14).

Over a wide range of oxygen chemical potentials the most favoured structure is, however, a surface terminated with vanadyl V=O groups. Such termination consists of a (1 × 1) unit cell with respect to the bulk structure with a further oxygen atom bonded to the outermost vanadia atom. Experiments confirm this theoretical prediction [42]. Figure 6.15 shows vibrational spectra of different vanadia films deposited on Rh(111). Spectrum (a) is recorded for a film exhibiting the (1 × 1) structure: it is characterised by features at 47, 78, and 129 meV, a weak shoulder at 92 meV and a weak structure at 156 meV. The losses at energies lower than 100 meV are associated to the phonons of V_2O_3. Theory predicts modes of relevant intensity under dipole scattering conditions at 46.2 and 63.3 meV (motion orthogonal to the hexagonal planes), a mode at 82 meV (originating from three oxygen atoms below the V=O group, vibrating nearly normally to the surface) and a mode at 135 meV (due to the vanadyl stretching mode, as suggested also by its high energy). The presence of the 129 meV vibration, close to the value predicted for the vanadyl stretch, provides a strong evidence for the presence of V=O groups. The spectrum is analogous to the one observed for a 5 ML thick film of vanadium oxide grown on Pd(111) [46].

Exposing the vanadyl terminated (1 × 1) surface to oxygen (5 × 10^6 mbar) at 500 °C leads to the formation of a well ordered $(\sqrt{3} \times \sqrt{3})R30°$ surface (see model

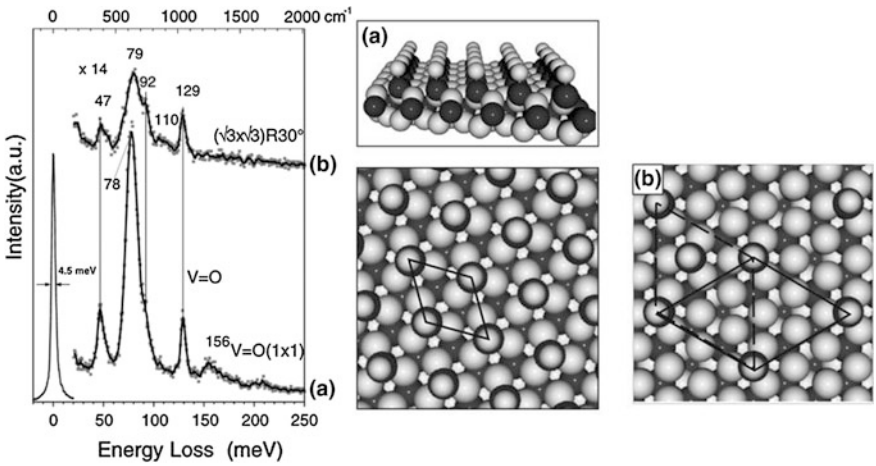

Fig. 6.15 *Left* HREEL spectra of the: **a** V_2O_3 (0001)(1 × 1) and **b** $(\sqrt{3} \times \sqrt{3})R30°$ surfaces recorded at 300 K. *Center* Model of the (1 × 1) surface: *dark spheres* indicate vanadium atoms while *bright ones* represent oxygen atoms. *Right* Model of the $(\sqrt{3} \times \sqrt{3})R30°$ structure with unit cells containing one (*dashed*) or two (*solid*) missing vanadyl groups. Taken with permission from [42]. DOI: 10.1088/0953-8984/17/26/004

in the right part of Fig. 6.15). Due to the removal of V=O groups the surface layer is now oxygen richer. The corresponding vibrational spectrum is not very different from the one proper of the (1 × 1) structure, except for the overall lower intensity and for an additional loss at 110 meV which is not assigned. The similarity is explained by the close values of the vibrational modes of the O_3 terminated surface and to the residual presence of V=O groups [45].

Vanadium oxide films were grown also on TiO_2 [44]. In this case the vibrational spectra are complicated by the presence of the phonon modes of titania. The data analysis is therefore based on difference spectra, which confirm the assignments given above (see Fig. 6.16). The major difference is the observation of a peak at 111 meV rather than at 129 meV. The smaller frequency indicates the formation of a reactive oxygen species (VO_r bond rather than V=O), which is present on VO_x strands as well as on nanoislands.

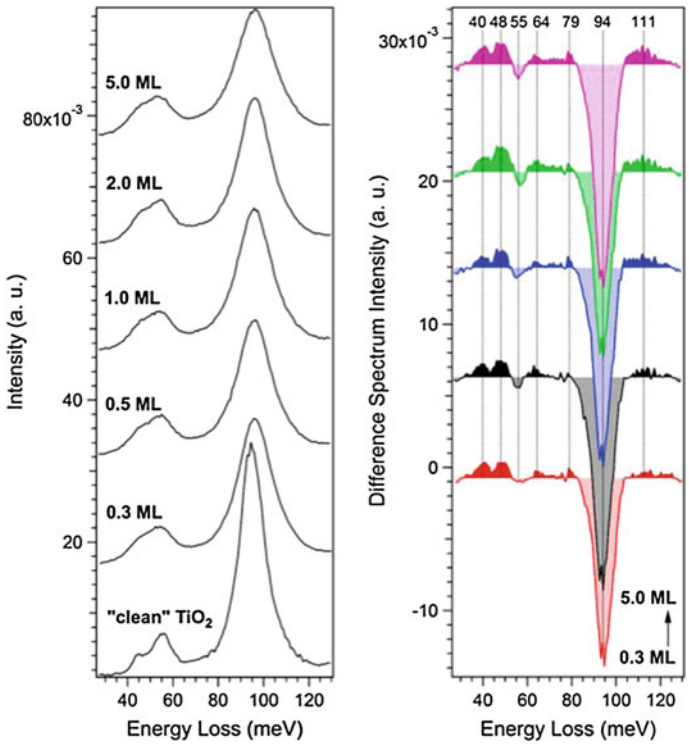

Fig. 6.16 VO_x (0.35.0 ML)/TiO_2(110) thin films. **a** HREELS data (recorded in specular) and **b** HREELS difference spectra calculated by subtracting the clean TiO_2(110) spectrum. Taken with permission from [44]. Copyright by ACS

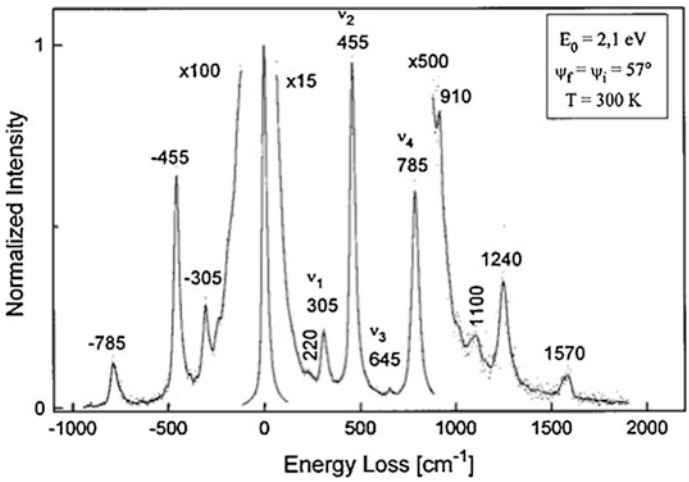

Fig. 6.17 HREEL spectra of β-Ga_2O_3 grown on CoGa(100). Taken with permission from [47]. Copyright by AIP

6.5.5 Ga_2O_3

In Fig. 6.17 we show HREEL spectra recorded for a 15 Å thick film of Gallium oxide (β-Ga_2O_3) grown on CoGa(100) (an intermetallic alloy, similar to NiAl) [47]. Losses at 220 cm^{-1} (27 meV) (extremely faint), 305 cm^{-1} (38 meV, ν_1), 455 cm^{-1} (56 meV, ν_2), 645 cm^{-1} (80 meV, ν_3) and 785 cm^{-1} (97 meV, ν_4) are observed together with the corresponding gain peaks and losses due to multiple excitation. Such losses correspond to the FK modes and are in good agreement with the values estimated theoretically on the base of dielectric theory.

The parameters used in this calculation are close to those of bulk Ga_2O_3 with the only exception of $\omega_{TO,3}$ (620 cm^{-1} (77 meV) in the model used in [47] to be compared with 450 cm^{-1} (56 meV) for the bulk oxide). The discrepancy may be due do the low thickness of the film, in which the top and bottom layers are slightly distorted with respect to their bulk counterpart.

6.5.6 CeO_2

Vibrational spectroscopy has also been used to assess the stoichiometry of cerium and chromium oxide films. Three cerium oxide bulk structures of defined stoichiometry are known: CeO_2, hexagonal h-Ce_2O_3 and cubic c-Ce_2O_3 [48].

CeO_2, which is the most common phase also known as ceria, crystallizes in a fluorite type structure with a lattice constant of 5.41 Å. The left panel of Fig. 6.18 shows the HREEL spectrum recorded after oxidising at 1000 K a Pt_xCe-Pt(111)

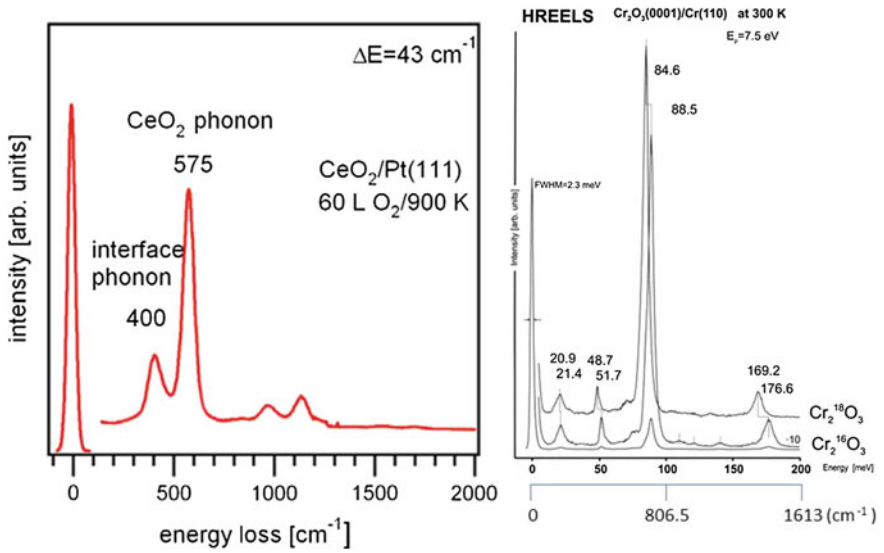

Fig. 6.18 *Left* HREEL spectra recorded for a ceria film (see text for details). *Right* HREEL spectra recorded for a Cr_2O_3 film of thckness ≈40 Å grown on Cr(110). Taken with permission from [48, 49]. Copyright by Elsevier

surface alloy, obtained evaporating Ce on a Pt(111) single crystal. Films of thickness between 1 and 5 layers were obtained. Two modes are evident: at 400 cm^{-1} (50 meV) and 575 cm^{-1} (72 meV). The former loss is due to an interface phonon while the latter is a phonon of the overlayer. This assignment is supported by the fact that the intensity of the high frequency mode increases with increasing thickness.

The comparison with vibrational data recorded for Cr_2O_3 grown on Cr(110) [49] (right panel of the same figure) allows to exclude the formation of h-Ce_2O_3 : in this case similar spectra should be obtained, contrary to experimental evidence.The film has thus a fluorite type CeO_2(111) structure.

6.5.7 Cr_2O_3

For Cr_2O_3 the main modes are observed at 417 cm^{-1} (51.7 meV), 634 cm^{-1} (78.6 meV) and 714 cm^{-1} (88.5 meV) and correspond to three of the six expected dipole active modes [50] of the bulk oxide surface. They are thus identified with FK modes. The shoulder of the peak at 88.5 meV was tentatively ascribed to a further FK mode. The mode at 21.4 meV was assigned to a vertical in-phase vibration of the outermost O layer and the two Cr layers below while the higher frequency modes are due to combination losses.

6.6 Me_3O_4 and More Complex Oxides

6.6.1 Fe_3O_4

Fe_3O_4 films grown on alumina have been investigated by Raman Spectroscopy [51]. Iron oxides exist in different stoichiometry and structures: magnetite, hematite (α-Fe_2O_3), maghemite (γ-Fe_2O_3) and würstite ($Fe_{1-x}O$). Distinguishing among them is not straightforward: e.g. magnetite and maghemite have a similar crystal structure and close lattice constants.

Although the selection rules for RS and IR spectroscopy are quite different, vibrational information obtained from RS can also be used to distinguish between such crystallographic phases. By using group theory, it is indeed possible to predict

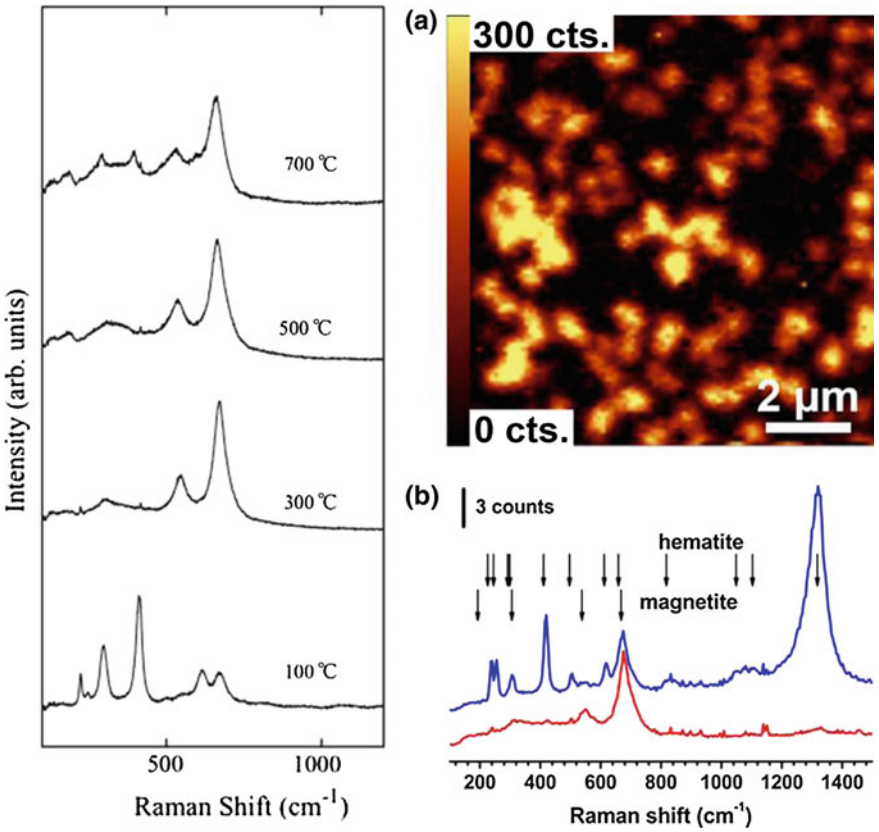

Fig. 6.19 *Left* Raman shift for Fe_3O_4 film grown on α-Al_2O_3. Taken with permission from [51]. Copyright by Elsevier. *Right* Raman image (**a**) and Raman shift (**b**) distinguishing bright areas (*blue line*, hematite) from dark ones (*red line*, magnetite). Taken with permission from [52]. Copyright by Elsevier

the number and symmetry of Raman active modes while the comparison with literature provides the frequency of the modes observed for magnetite and hematite [52].

Figure 6.19 shows the evolution of Raman spectra obtained growing the Fe_3O_4 film on the same substrate at different temperatures. In the film grown at 100 °C the vibrational features of both magnetite and hematite are present while at higher temperatures (300 and 500 °C) the intensities of the modes due to hematite decrease in favour of those due to magnetite. Only at 700 °C the features associated to hematite appear again.

At the lowest temperature adatom migration is slow and then crystals of poor quality are obtained. Increasing the temperature the quality improves. The negative effect of a further increase in the substrate temperature was explained as due to re-evaporation of the adatoms of the substrate.

6.6.2 Mn_3O_4

Mn_3O_4 thin films have been grown on Rh(111) [53]. Mn is thereby first evaporated on the Rh(111) substrate at RT and then oxidised at different temperatures. The corresponding HREEL spectra, shown in Fig. 6.20, should be compared with those of *MnO* reported in Figs. 6.2 and 6.3. Independently of the thickness of the film, peaks at ≈47 and 80 meV (379 and 645 cm^{-1}, respectively) appear already at the lowest temperature and slightly upshift in energy with increasing oxidation temperature. Such peaks are indicative of a trilayer O–Mn–O structure. For thicknesses of 2 and 3 ML, new loss peaks show up at 13, 39, 68 and 83 meV (105, 315, 548 and 669 cm^{-1}, respectively), such peaks being better resolved when oxidising Mn at 700 K or at 800 K. Since these peaks are indicative of a Mn_3O_4 structure, we can conclude that the latter forms only for films thicker than 1 ML.

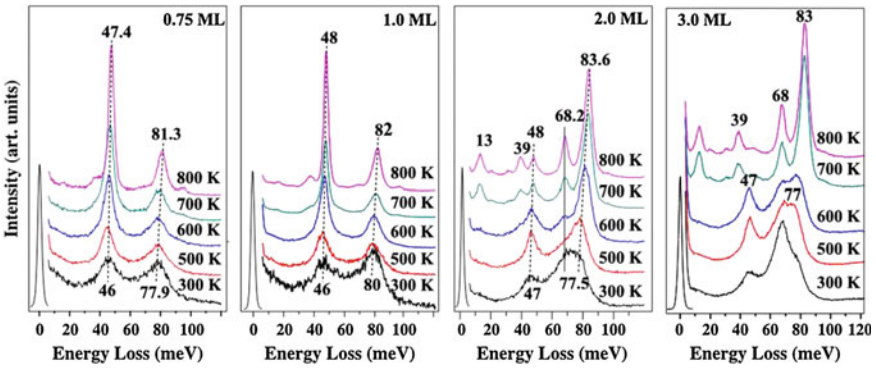

Fig. 6.20 HREEL spectra recorded for manganese oxide films of different thicknesses (0.75, 1, 2 and 3 ML) obtained by oxidising at the indicated temperature a Mn film deposited at RT. Taken with permission from [53]. Copyright by Elsevier

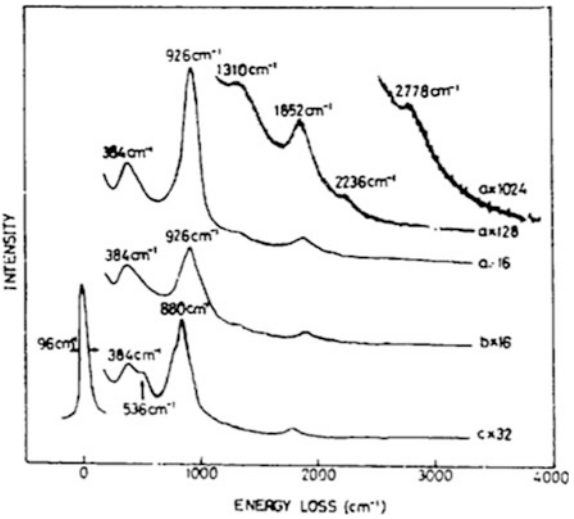

Fig. 6.21 HREEL spectra recorded for **a** a NbO thin film (3 ML), **b** a Nb_20_5 thin film (3 ML) and **c** after bombarding Nb_20_5 film with Ar ions to remove one layer. Taken with permission from [54]. Copyright by Elsevier

6.6.3 Niobium Oxide

As an example of more complex oxides, we show in Fig. 6.21 the HREEL spectra recorded for films of niobia with different stoichiometry, obtained by depositing Nb on Pt(111) and oxidising it [54]. Niobia may indeed grow in at least three possible stoichiometries: NbO, NbO_2 and Nb_2O_5.

NbO_x is obtained after an exposure of 500 L oxygen per 0.1 monolayer of Nb. Nb_2O_5 forms for an exposure of 1200 L O_2 at the same Nb coverage. The spectra for these films exhibit similar frequencies suggesting the presence of a common building block. The comparison of HREELS data for the film with data for the bulk crystal surface lead Xie et al. to conclude that the crystal structure(s) of the film do not correlate with the structures of bulk terminated oxides of niobium. The peak at 928 cm^{-1} (115 meV) was assigned to terminal Nb=O surface sites of highly distorted NbO_6 octahedra.

After Ar bombardment the film is characterized by the appearance of a new loss feature at 536 cm^{-1} (66 meV), which indicates the presence of a still different phase, explained by the formation of oxygen vacancies with the reduced niobium atoms.

6.6.4 Ternary Oxides

Little work is present in literature on thin films of ternary oxides. Tungstates ($MeWO_4$) have been recently studied because of their high potential in optics, optoeletronics and photochemistry. Denk et al. [55] succeeded recently to grow

films of such compound with atomic control by depositing $(WO_3)_3$ clusters on Cu (110) − (2 × 1)O at cryogenic crystal temperatures. A morphologically flat and well ordered W oxide overlayer is then obtained upon annealing a full monolayer of such molecules at 600 K. As shown in Fig. 6.22 HREELS losses are apparent at ≈860 and 960 cm^{-1}. In bulk WO_3 the W–O–W groups cause bands at 711 and 806 cm^{-1} (88 and 100 meV, respectively) while a band at 987 cm^{-1}, (122 meV) is indicative of the presence of W=O (tungstyls). DFT calculations indicate, however, that for the oxide film the highest observed frequency may correspond to the W–O stretching of WO_4 tetrahedra (found theoretically at 935 cm^{-1}, 116 meV) rather than to tungstyl. The eigenvectors of this vibration are reported in Fig. 6.22b.

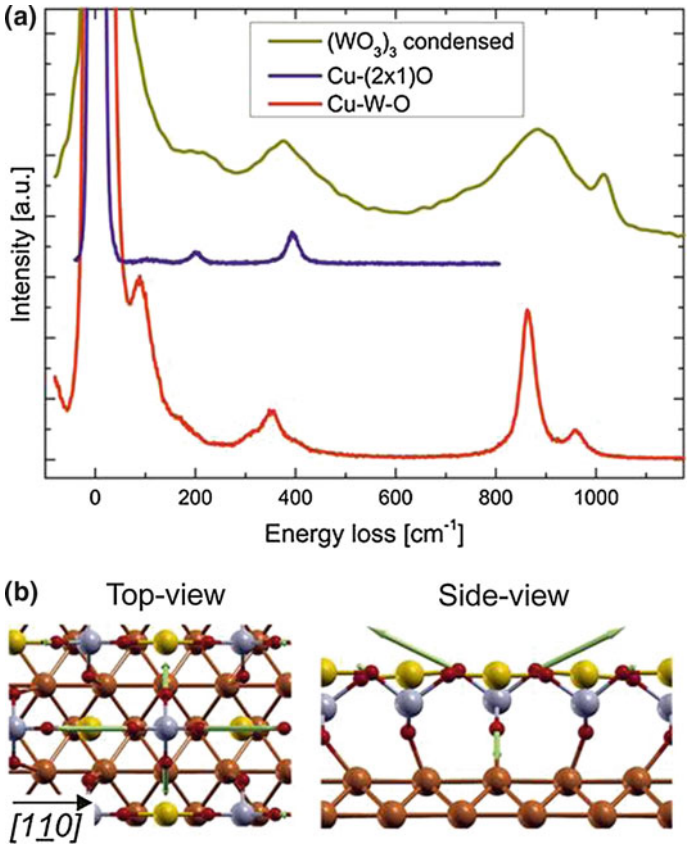

Fig. 6.22 **a** HREEL spectrum of the 2-D $CuWO_4$ system (Cu–W–O, in *red*), compared to the Cu - (2 × 1)O bare substrate (in *blue*) and to a thick film of $(WO_3)_3$ clusters (in *green*). **b** Top and side views of the high-frequency vibrational mode at 935 cm^{-1} as predicted by DFT. The *green arrows* indicate the direction of atomic displacements. Taken with permission from [55]. Copyright by ACS

Ultrathin films of $BaTiO_3$(001) were recently grown on Pt(001) by the group of Widdra [56, 57], who also performed HREELS investigations which are, however, still unpublished.

6.7 Conclusions

We have presented selected examples showing how vibrational spectroscopy has been used to determine the nature (stoichiometry and symmetry) and in some cases even the morphology of thin oxide films. The assignment of the observed vibrational signatures is non trivial and is ultimately based on symmetry arguments and on the selection rules operative for the probe particles (electrons or photons), for the particular substrate (metallic or not) and for the given scattering geometry.

While for thick enough thin films the predictions of macroscopic dielectric theory are generally confirmed by experiments, in the ultrathin limit microscopic modes are also observed and for their assignment a theory is usually required.

Once the more general properties of the film have been established, comparison of the frequencies and of the intensities of the modes for different growth conditions can provide information about the morphology of the film and about the different phases which may form. Vibrational analysis can highlight, moreover, the growth mode (layer by layer vs. 3D), thus complementing the information provided by microscopy.

Acknowledgements We thank Compagnia San Paolo for funding this research.

References

1. Honkala K (2014) Tailoring oxide properties: an impact on adsorption characteristics of molecules and metals. Surf Sci Rep 69:366–388
2. Freund HJ, Pacchioni G (2008) Oxide ultra-thin films on metals: new materials for the design of supported metal catalysts. Chem Soc Rev 37:2224–2242
3. Goodman W (1995) Model studies in catalysis using surface science probes. Chem Rev 95:523–536
4. Fuchs R, Kliewer KL (1965) Optical modes of vibration in an ionic crystal slab. Phys Rev 140:A2076–A2088
5. Cox PA, Hill MD, Peplinskii F et al (1984) 2D surface phonons in high-resolution electron-energy-loss spectra of metallic oxides. Surf Sci 141:13–30
6. Sachert S, Polzin S, Kostov K et al (2010) Thickness dependent vibrational and electronic properties of MnO(100) thin films grown on Pt(111). Phys Rev B 81:195424-1–195424-7
7. Frederick BG, Apai G, Rhodin TN (1991) Surface phonons in thin aluminum oxide films: thickness, beam-energy, and symmetry-mixing effects. Phys Rev B 44:1880–1890
8. Lambin Ph, Senet P, Lucas AA (1991) Validity of the dielectric approximation in describing electron-energy-loss spectra of surface and interface phonons in thin films of ionic crystals. Phys Rev B 44:6416–6428

9. Ibach H, Mills DL (1982) Electron energy loss specroscopy and surface vibrations. Academic Press, New York
10. Hoffmann FM (1983) Infrared reflection-absorption spectroscopy of adsorbed molecules. Surf Sci Rep 3:109–192
11. Siebert F, Hildebrandt P (2008) Vibrational spectroscopy in life sciences. Wiley-VCH Verlag GmbH and Co. KGaA, Weinheim. doi:10.1002/9783527621347.ch2
12. Xu ML, Hall BM, Tong SY et al (1985) Energy dependence of inelastic electron scattering cross section by surface vibrations: experimental measurement and theoretical interpretation. Phys Rev Lett 54:1171–1174
13. Rocca M, Ibach H, Lehwald S et al (1986) Surface phonon dispersion of surface and adsorbate layers. In: Von Blanckenhagen P, Schommers W (eds) Structure and dynamics of surfaces. Topics in current physics, vol 41. Springer, Berlin, pp 245–276
14. Agarwal SK (1979) Lattice-dynamics of transition metal oxides MnO and NiO. Solid State Comm 29:197–200
15. Rudolf T, Kant Ch, Mayr F et al (2008) Magnetic-order induced phonon splitting in MnO from far-infrared spectroscopy. Phys Rev B 77:024421-1–024421-5)
16. Savio L, Celasco E, Vattuone L et al (2003) MgO/Ag(100): confined vibrational modes in the limit of ultrathin films. Phys Rev B 67:075420-1–075420-5
17. Pal J, Smerieri M, Celasco E et al (2014) Morphology of monolayer MgO films on Ag(100): switching from corrugated islands to extended flat terraces. Phys Rev Lett 112:126102-1–126102-5
18. Pal J, Smerieri M, Celasco E et al (2014) How growing conditions and interfacial oxygen affect the final morphology of MgO/Ag(100) films. J Phys Chem C 118:26091–26102
19. Hwang Y, Souda E, Aizawa T et al (1997) Surface phonon of MgO layer on TiC(100) surface. Jpn J Appl Phys 36:5707–5708
20. Schoiswohl J, Agnoli S, Xu B et al (2005) Growth and thermal behaviour of NiO nanolayers on Pd(1 0 0). Surf Sci 599:1–13
21. Tyuliev GT, Kostov KL (1999) XPS/HREELS study of NiO films grown on Ni(111). Phys Rev B 60:2900–2907
22. Cox PA, Williams AA (1985) The observation of surface optical phonons and low-energy electronic transitions in NiO single crystals by electron energy loss spectroscopy. Surf Sci 152 (153):791–796
23. Le Moal S, Moors M, Essen JM et al (2013) Structural and compositional characterization of ultrathin titanium oxide films grown on $Pt_3Ti(111)$. J Phys Cond Matt 25:045013-(1–11)
24. Langell MA, Hutchings CW, Carson GA et al (1996) High resolution electron energy loss spectroscopy of MnO(100) and oxidized MnO(100). J Vac Sci Technol A 14:1656–1661
25. Wulser KW, Langell MA (1994) Fuchs-Kliewer phonon structure and surface integrity of NiO (100). Surf Sci 314:385–397
26. Carson GA, Nassir MH, Langell MA (1996) Epitaxial growth of Co_3O_4 on CoO(100). J Vac SciTechnol A 14:1637–1642
27. Guo Q, Oh WS, Goodman DW (1999) Titanium oxide films grown on Mo(110). Surf Sci 437:49–60
28. Henderson MA (1996) An HREELS and TPD study of water on TiO_2(110): the extent of molecular versus dissociative adsorption. Surf Sci 355:151–166
29. Gunrick G, Poelman H, Clauws P et al (1991) Observation of surface phonons on the (001) and (100) surfaces of anatase minerals. Solid State Comm 80:579–581
30. Chen MS, Santra AK, Goodman DW (2004) Structure of thin SiO_2 films grown on Mo(112). Phys Rev B 69:155404-1–155404-7)
31. Wendt S, Ozensoy E, Wei T et al (2005) Electronic and vibrational properties of ultrathin SiO_2 films grown on Mo(112). Phys Rev B 72:115409-1–115409-9
32. Kaya S, Baron M, Stacchiola D et al (2007) On the geometrical and electronic structure of an ultra-thin crystalline silica film grown on Mo(1 1 2). Surf Sci 601:4849–4861
33. Schroeder T, Giorgi JB, Bäumer M et al (2002) Morphological and electronic properties of ultrathin crystalline silica epilayers on a Mo(112) substrate. Phys Rev B 66:165422-1–165422-11

34. Lu JL, Kaya S, Weissenrieder J et al (2006) Formation of one-dimensional crystalline silica on a metal substrate. Surf Sci 600:L164–L168
35. Frank M, Wolter K, Magg N et al (2001) Phonons of clean and metal-modified oxide films: an infrared and HREELS study. Surf Sci 492:270–284
36. Berreman DW (1963) Infrared absorption at longitudinal optic frequency in cubic crystal films. Phys Rev 130:2193–2198
37. Franchy R (2000) Growth of thin, crystalline oxide, nitride and oxynitride films on metal and metal alloy surfaces. Surf Sci Rep 38:195–294
38. Strong RL, Firey B, de Wette FW et al (1982) Surface-site determination using electron-energy-loss spectroscopy and lattice-dynamical models. Phys Rev B 26:3483(R)-3486 and its Erratum Phys Rev B 27:3896
39. Lee MB, Lee JH, Frederick BG et al (2000) Surface structure of ultra-thin Al_2O_3 films on metal substrates. Surf Sci 448:L207–L212
40. Franchy R, Masuch J, Gassmann P (1996) The oxidation of the NiAl(111) surface. App Surf Sci 93:317–327
41. Gassmann P, Franchy R, Ibach H (1994) Investigations on phase transitions within thin Al_2O_3 layers on NiAl(001) HREELS on aluminum oxide films. Surf Sci 319:95–109
42. Pfuner F, Schoiswohl J, Sock M et al (2005) The metalinsulator transition in V_2O_3(0001) thin films: surface termination effects. J Phys Cond Matt 17:4035–4047
43. Guo K, Lee S, Goodman DW (1999) Vanadium oxides thin films grown on rutile TiO_2(110)-(1 1)and(1 × 2) surfaces. Surf Sci 437:38–48
44. Artiglia L, Agnoli S, Savio L et al (2014) From Vanadia nanoclusters to ultrathin films on TiO_2(110): evolution of the yield and selectivity in the ethanol oxidation reaction. ACS Catal 4:3715–3723
45. Kresse G, Surnev S, Schoiswohl J et al (2004) V_2O_3(0001) surface terminations: a density functional study. Surf Sci 555:118–134
46. Surnev S, Kresse G, Sock M et al (2001) Surface structures of ultrathin vanadium oxide films on Pd(1 1 1. Surf Sci 495:91–106
47. Schmitz G, Gassmann P, Franchy R (1998) A combined scanning tunneling microscopy and electron energy loss spectroscopy study on the formation of thin, well-ordered β-Ga_2O_3 films on CoGa(001). J Appl Phys 83:2533–2538
48. Breinlich C, Essen JM, Barletta E et al (2011) Growth, structure and electronic properties of ultrathin cerium oxide films grown on Pt(111). Thin Solid Films 519:3752–3755
49. Wolter K, Scarano D, Fritsch J et al (2000) Observation of a localized surface phonon on an oxide surface. Chem Phys Lett 320:206–211
50. Renneke DR, Lynch DW (1965) Infrared lattice vibrations and dielectric dispersion in single-crystal Cr_2O_3. Phys Rev 138:A530–A533
51. Ding J, Zhang D, Arita M et al (2011) Growth and characterization of Fe_3O_4 films. Mat Res Bull 46:2212–2216
52. Lübbe M, Gigler A, Stark R et al (2010) Identification of iron oxide phases in thin films grown on Al_2O_3(0001) by Raman spectroscopy and X-ray diffraction. Surf Sci 604:679–685
53. Zhang L, Tang Z, Wang S et al (2012) Growth and vibrational properties of MnO_x thin films on Rh(111). Surf Sci 606:1507–1511
54. Xie L, Wang D, Zhong C et al (1994) The preparation of and water adsorption on thin films of niobium oxide on Pt(111). Surf Sci 320:62–76
55. Denk M, Kuhness D, Wagner M et al (2014) Metal tungstates at the ultimate two-dimensional limit: fabrication of a $CuWO_4$ nanophase. AcsNano 8:3947–3954
56. Förster S, Meinel K, Hammer R et al (2013) Quasicrystalline structure formation in a classical crystalline thin-film system. Nature 502:215–218
57. Widdra W, Schumann F, Christl M et al (2015) Surface phonons and ferroelectric coupling in ultrathin perovskite oxides. ECOSS 31 Book of abstract, 129, available at: http://www.ecoss2015.org